

Aeolian driven oxidant and hydrogen generation in Martian regolith: The role of mineralogy and abrasion temperature

John O. Edgar ^a, Katie Gilmour^b, Maggie L. White^b, Geoffrey D. Abbott^a, Jon Telling^{a*}

^a School of Natural and Environmental Sciences, Newcastle University, Newcastle upon Tyne, NE1 7RU, UK

^b School of Engineering, Newcastle University, Newcastle upon Tyne, NE1 7RU, UK

*Corresponding author email address: jon.telling@newcastle.ac.uk

Abstract

1. Introduction
2. Methods
 - 2.1 Sample preparation & Identification
 - 2.2 Simulated Saltation
 - 2.3 Hydrogen peroxide determination
 - 2.4 Hydrogen determination
 - 2.5 Iron determination
3. Discussion
 - 3.1 The temperature dependence of mineral comminution
 - 3.2 Hydrogen peroxide generation
 - 3.3 Iron availability and Fenton chemistry
 - 3.4 Hydrogen generation
 - 3.5 Oxidant regulation of hydrogen generation
 - 3.6 Implications for Mars
 - 3.6.1 Water and oxygen availability as a control on ROS production
 - 3.6.2 Abrasion rate as a function of temperature
 - 3.6.3 Mineral structure and Fe content as controls on oxidant production
 - 3.6.4 The impact of aeolian driven oxidant production on organic matter preservation
 - 3.6.5 Insight into low temperature hydrogen generation
4. Conclusions
5. References

Abstract

The surface of Mars is a dynamic, cold environment where aeolian abrasion leads to the fracturing of silicate minerals which can produce oxidants upon exposure to water. Here we report results of a series of laboratory experiments where the abrasion of sand sized (125 – 300 μm) quartz, labradorite, forsterite and opal were conducted under a simulated Martian atmosphere at a range of temperatures common to Mars' surface (193 to 273 K). Our results suggest that abrasion rates are controlled by temperature; an observation that may have potential for providing insight into Martian paleo-temperatures. On the addition of water, detectable H_2O_2 was generated in all abraded experiments with crystalline quartz, labradorite and forsterite, but not amorphous opal – supporting previous inferences that mineral crystal structure plays a role in oxidant production. Dissolved Fe concentrations also indicated a strong additional control on net H_2O_2 production by Fenton reactions. Detectable H_2 was similarly measured in abraded experiments with crystalline minerals and not for amorphous opal. Labradorite and forsterite generated minimal H_2 and only in more abraded samples, likely due to the reaction of Si^\cdot with water. In quartz experiments H_2 was only present in samples where a black magnetic trace mineral was also present, and where H_2O_2 concentrations had been reduced to close to detection. In the quartz samples we infer a mechanism of H_2 generation via the previously proposed model of spinel-surface-promoted-electron transfer to water. The presence of H_2O_2 may exert an additional control on net H_2 production rates either directly (via reaction of H_2 with OH^\cdot and H_2O_2) or indirectly (by the oxidation of H_2 generating sites on mineral surfaces). Overall, our data supports previous inferences that aeolian abrasion can produce additional oxidants within the Martian regolith that can increase the degradation of organic molecules. We further suggest that the apparent control of H_2O_2 concentrations on net H_2 generation in our experiments may help explain some previous apparently contradictory evidence for mineral-water H_2 generation at low temperatures.

Keywords

Mars, aeolian abrasion, low-temperature, hydrogen peroxide, hydrogen, Fenton chemistry

1 Introduction

2 Over geological time large quantities of organic bearing meteoritic material should have been deposited
3 on the Martian surface; however, direct chemical analysis of Martian regolith has detected a maximum
4 of 24.4 ppm organic carbon by mass (Eigenbrode et al., 2018). Better understanding the mechanisms
5 that can alter and destroy organic molecules in Martian regolith can help us to constrain the preservation
6 potential of organic molecules of both abiotic and potentially biotic origin, as well as helping to evaluate
7 the sources of any organic material. Viking lander experiments found the regolith able to oxidise
8 nutrients (Levin & Straat, 1977) and release oxygen upon exposure to water (Oyama & Berdahl, 1977),
9 suggesting the presence of Reactive Oxygen Species (ROS). ROS were also inferred to be responsible
10 for the lack of detection of organic molecules (Bienmann et al., 1977). Hydrogen peroxide (H_2O_2) can
11 be produced photochemically in Mars' atmosphere (Atreya & Gu, 1994) and has been detected in the
12 atmospheric column (Encrenaz et al., 2004). Photochemical reactions involving mineral surfaces have

13 been invoked to explain the generation of ROS such as the superoxide radical (O_2^-) which can form on
14 labradorite surfaces when they are irradiated under analogue Martian conditions (Yen et al., 2000), and
15 perchlorates (ClO_4^-) detected in-situ on Mars by the Wet Chemistry Lab on board the Phoenix Mars
16 lander (Hecht et al., 2009).

17 Aeolian processes on Mars may further promote ROS production. Electrostatic fields can be generated
18 through triboelectric effects as wind driven dust storms propagate. This can result in the dissociation of
19 atmospheric CO_2 and H_2O , leading to the formation of new reactive chemical products (Delory et al.,
20 2006) and may produce significant quantities of H_2O_2 (Atreya et al., 2006). The saltation and
21 subsequent collision of sand particles may also generate additional ROS (Bak et al., 2017). Sand fluxes
22 on Mars have been shown to locally approach levels observed in cold, dry deserts on Earth (Bridges et
23 al., 2012). Analysis of predicted sand fluxes from climate models (Richardson et al., 2007) with
24 measured observations of dune and ripple migration suggest a sand mobility threshold for Mars of 0.82
25 $m\ s^{-1}$ (Ayoub et al 2014; Bridges et al., 2017). Numerical models suggest that sustained saltation is
26 possible where wind speeds remain close to the impact threshold without the requirement to
27 consistently reach or exceed the fluid friction threshold (Sullivan & Kok, 2017).

28 In prior low energy studies simulating Martian saltation, Bak et al. (2017) demonstrated that the high
29 CO_2 content of the Martian atmosphere inhibited the direct production of H_2O_2 on mineral surfaces,
30 although significant generation of H_2O_2 still took place. The H_2O_2 in these experiments was instead most
31 likely produced by triboelectrically induced reactions promoted by the low Martian pressures (Bak et al.,
32 2017). This study was however conducted with limited materials (quartz and basalt) and with abrasion
33 at ambient room temperature; much warmer than average Martian temperatures (Martínez et al., 2017).

34 Here we extend our understanding of ROS production by sand abrasion in Martian regolith by assessing
35 not only a greater range of analogue Martian minerals (quartz, labradorite, forsterite, opal) on H_2O_2
36 generation, but also the effect of the temperature of abrasion on oxidant production. We further couple
37 measurements of H_2O_2 to simultaneous measurements of H_2 to gain greater insight into the
38 mechanisms of coupled oxidant-hydrogen generation from abraded mineral-water reactions. Minerals
39 were abraded under an analogue Martian atmosphere at a range of temperatures (193 to 273 K) likely
40 to be encountered on the Martian surface. Generation of H_2O_2 and H_2 was monitored in time series
41 after the addition of water, and the amount of dissolved Fe was also recorded at the end of the
42 experiments.

43 2. Methods

44 2.1 Sample preparation & Identification

45 The quartz, labradorite and forsterite used in this study were commercially sourced from Northern
46 Geological Supplies Ltd, UK and the opal from Fantasia Mining, USA. Mineral phase identification (Figs.
47 S1 & S2) was performed by X-Ray Diffraction (XRD); full details are provided in Appendix A. Equi-
48 granular batches of each mineral were prepared by grinding in a ball mill and sieving to isolate the 125
49 to 300 μm size fraction. Minerals were then washed and sonicated in $18.2\ M\Omega\ cm^{-1}$ water to remove
50 any adhered fine material before oven drying at $70^\circ C$ for 48 hours. Submersion of silicate minerals in

51 water and subsequent drying has been shown to deplete the oxidant-producing surface silica radical
52 sites generated in the milling process (Bak et al., 2017).

53 Custom made quartz ampoules (100 mm long; Fig. S3) were washed in 0.6 M HCl, rinsed 5 × with
54 18.2MΩ cm⁻¹ water, then furnace at 500 °C for four hours. 10 g aliquots of each mineral were added
55 to ampoules in triplicate for each temperature point. Quartz wool (treated the same way as the
56 ampoules) was inserted at the ampoule constriction, followed by Belco butyl rubber stoppers (part no.
57 2048-11800A) that had previously been boiled in 1M NaOH for 1 hour then rinsed 5 × with 18.2MΩ cm⁻¹
58 water. Ampoules were then crimp sealed.

59 The ampoules were then connected to a vacuum/gassing line and evacuating to < 8 x 10⁻³ mbar,
60 monitored using an Edwards APG100-XM Active Pirani Gauge. 7.0 mbar of a gas mix containing 96.05
61 % CO₂, 1.9 % Ar, 1.9 % N₂ and 0.15 % O₂ was then introduced, measured by an Edwards ASG2 Active
62 Strain Gauge. This gas mixture replicates the mixing ratios in the Martian near surface atmosphere as
63 measured by the SAM instrument on Curiosity (Mahaffy et al., 2013). Non-abraded controls for each
64 mineral at the four temperatures were prepared in an identical way (n = 48; Appendix B), alongside
65 water-only procedural blanks (n=24).

66 2.2 Simulated Saltation

67 A rig to mechanically abrade granular material under conditions simulating saltation was developed
68 following Merrison (2012). Ampoules were fastened tangentially to discs pinned to an axle rotating at
69 40 rpm. Each full rotation causes two inversions of the ampoule resulting in the contents falling from
70 one end to the other under gravity. The velocity of the mineral particles at impact was ~ 1 m s⁻¹ which
71 represents saltation impact velocities at low mobilisation rates, close to the saltation threshold
72 (Merrison, 2012). For a 142-day experiment this equates to ~ 16 x 10⁶ inversions. The mechanical
73 power input of each inversion can be approximated as the specific gravitational energy (E_u) of the grains
74 as they fall the length of the ampoule (h) under gravity (g), corresponding in this instance to ~ 0.8 W
75 Kg⁻¹. The power transferred from the wind to grains at the threshold of saltation has been estimated to
76 be ~ 0.05 W Kg⁻¹ (Iversen and Rasmussen, 1999; Merrison, 2012), hence our experiments simulate ~
77 6 years of continuous sand mobilisation at threshold wind speeds.

78 The rigs were housed and operated within incubators for temperature control. Incubators had side ports
79 allowing the rotator axle through the wall leaving the motor outside at room temperature (Fig. S4).
80 Temperatures within incubators were monitored with temperature probes connected to an Omega OM-
81 CP series data logger. Non-abraded mineral controls were placed in the same incubators for an identical
82 time period, but without rotation, and water-only controls were also run in both rotating and non-rotating
83 configurations.

84 After simulated saltation, all ampoules were warmed to 293 K and 20 mL of 5.0 grade He gas was
85 added using a gas tight syringe. 10 mL of He sparged water was then added and well mixed with any
86 excess gas equilibrated to atmospheric pressure. Oxygen levels in the water prior to addition were
87 below 1.44 μmol L⁻¹ (~ 0.05 mg L⁻¹), monitored with a PreSens oxygen dipping probe (DP-PSt3).

88 2.3 Hydrogen peroxide determination

89 H₂O₂ concentrations were analysed following Baga et al. (1988). The procedure utilises the reduction
90 of copper (II) ions in the presence of 2,9-dimethyl-1,10-phenanthroline (DMP) forming the copper (I) –
91 DMP complex, Cu(DMP)²⁺. At each time point 1.5 mL of helium sparged water was added to the
92 ampoule using a syringe and needle and well mixed. 1.5 mL was then removed and filtered through a
93 0.2 µm nylon syringe filter, and 1 mL of this used in the assay.

94 A 1000 µmol L⁻¹ H₂O₂ stock was prepared from a 30 % w/w H₂O₂ solution and from this, a range of
95 fresh standards were diluted in the linear range 1 - 200 µmol L⁻¹ for each day of analysis. Measured
96 standards had a maximum coefficient of variance of 6.4 %. The method detection limit (MDL, based on
97 3 × SD of water-only controls) was 2.9 µmol L⁻¹. H₂O₂ concentrations are reported as the measured
98 H₂O₂ concentration from each abraded sample minus the average H₂O₂ concentration of three non-
99 abraded mineral controls stored at the same temperature.

100 2.4 Hydrogen determination

101 Gas samples were taken at 0, 24 and 168 hours. For each gas analysis, 4 mL of He was added to the
102 ampoule and the syringe pumped three times, then 4 mL of gas injected into a 3 mL Exetainer for
103 analysis. H₂ concentrations in the range 0 - 100 ppm were analysed on a ThermoFisher Gas
104 Chromatograph Pulsed Discharge Detection (GC-PDD) with a 2 m micropacked Shin Carbon ST
105 100/120 mesh, 1.0 mm ID column, with a constant flow (10 mL⁻¹) of helium carrier gas, column
106 temperature of 60°C and detector temperature of 110°C. Sample concentrations were calculated from
107 multiple dilutions of a 100 ppm certified standard in evacuated Exetainers (linear over 5 – 100 ppm, R²
108 = 0.99, n = 15). Standards were run before and after each day of analysis with a coefficient of variation
109 of 7.3 % (n = 86). The analytical detection limit was 1.4 nmol g⁻¹ and the MDL was 2.2 nmol g⁻¹. Gas
110 concentrations were calculated using the Ideal Gas Law, corrected for dilutions made during sampling
111 and normalised to the starting dry mass of the minerals, H₂ concentrations are reported as the measured
112 value from each abraded sample minus the average H₂ concentration of the specific non-abraded
113 mineral controls.

114 2.5 Iron determination

115 Dissolved Fe²⁺ and Fe³⁺ concentrations were sequentially determined in the range 0 – 20 µmol L⁻¹
116 utilising a revision of the ferrozine (the monosodium salt hydrate of 3-(2-pyridyl)-5,6-diphenyl-1,2,4-
117 triazine-p,p'disulphonic acid) spectrophotometric method following Viollier et al. (2000). Standards from
118 0 – 20 µmol L⁻¹ were prepared from a 1000 µg mL⁻¹ Fe³⁺ stock solution (1.79 × 10⁻² mol L⁻¹ of FeCl₃ in
119 10⁻² mol L⁻¹ HCl). The MDL was 0.03 µmol L⁻¹ and the maximum coefficient of variance after 5 repetitions
120 of each standard solution in the range 0 – 20 µmol L⁻¹ was 18.7 % (n= 34).

121 3. Results & Discussion

122 3.1 The temperature dependence of mineral comminution

123 These experiments were conducted under a range of temperatures encompassing the diurnal and
124 seasonal variations recorded *in situ* at a number of geographically distinct locations on Mars (193 K –
125 273 K; Martínez et al., 2017). Importantly, mechanical properties of minerals exhibit variability with
126 temperature (Weigle, 1949; Evans & Goetz, 1979; Kranjc et al., 2016), suggesting that temperature
127 should affect rates of mineral abrasion. In general, our experimental results support this.

128 After 142 days of simulated saltation all samples, at all temperatures, had been significantly reduced
129 from their starting grain size (Fig. 1). The amount of comminution was recorded as the mass of grains
130 under the lowest starting grain size of (125 μm) and given as a percentage of the total mass of material.
131 Quartz exhibited the least resistance to abrasion, producing the most fine material at both the warmest
132 and coldest temperatures (15.8 ± 2.2 and 11.0 ± 0.2 % respectively; $\pm 1\text{SD}$, $n = 3$); labradorite produced
133 the least material $< 125 \mu\text{m}$ (12.3 ± 2.6 and 9.3 ± 0.5 %; $\pm 1\text{SD}$, $n = 3$), whilst the amount of fine material
134 abraded from opal was consistently between those of quartz and labradorite at the warmest and coldest
135 temperatures (13.2 ± 0.8 and 11.2 ± 2.7 % respectively; $\pm 1\text{SD}$, $n = 3$). Hurowitz et al. (2007) found that
136 1.5 minutes of crushing in a swing mill produced surface areas for quartz and feldspar of 0.90, and 0.73
137 $\text{m}^2 \text{g}^{-1}$ respectively, suggesting mechanical properties of minerals in agreement with the results
138 presented here.

139 We note that our measurements were taken at the end of the experiment cycle after the minerals had
140 been exposed to water for over one week. Resultantly, minerals may have undergone varying degrees
141 of dissolution, and given that different minerals have different dissolution rates, the data presented in
142 Fig. 1 must be interpreted cautiously. Forsterite appears to have produced less than 10 % fines in 66
143 % of the experiments and shows no significant correlation ($r_s = -0.24$, $n = 12$, $p = 0.46$) with temperature.
144 The Goldich dissolution series ranks minerals in stability against weathering (Goldich 1938) in the order:
145 quartz – labradorite – forsterite which is the same order as the level of correlation for each of our major
146 rock forming minerals ($r_s \text{ quartz} = 0.86$, $p < 0.001$; $r_s \text{ labradorite} = 0.75$, $p < 0.01$; $r_s \text{ forsterite} = -0.24$, $p = 0.46$;
147 Fig. 1) perhaps suggesting dissolution processes have been active. In previous tumbling experiments
148 the surface area of abraded minerals has been shown to increase with increased duration of tumbling
149 (Bak et al., 2017). Tumbling experiments conducted by Merrison (2012), showed the generation of sub-
150 micron dust, whilst the distribution of the sand sized fraction remained largely unaltered. The dust
151 fraction will dominate the total surface area; accordingly, the surface area of our samples should also
152 have increased with the amount of comminution, and hence with the temperature of abrasion. An
153 interesting artefact of this method of simulating aeolian abrasion is the formation of dust agglomerates
154 (Merrison, 2012; Nørnberg et al., 2014). We did not observe this phenomenon due to conducting our
155 experiments wholly within the ampoules to ensure environmental control.

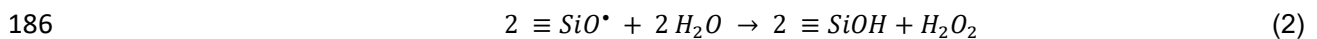
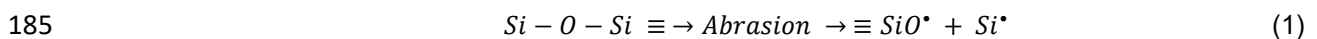
156 3.2 Hydrogen peroxide generation

157 After exposure to water, each mineral type except opal generated detectable quantities of H_2O_2 (MDL
158 = $2.9 \mu\text{mol L}^{-1}$; Figs. 2 & 3). The average peak H_2O_2 concentration was recorded in labradorite samples
159 ($117 \pm 18.0 \text{ nmol g}^{-1}$; Figs. 2 & 3) with a slightly lower average for quartz ($113 \pm 28.6 \text{ nmol g}^{-1}$; Figs. 2

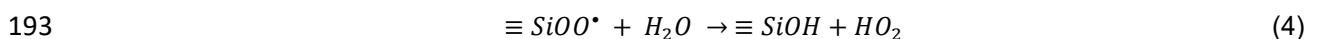
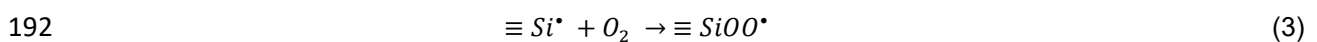
160 & 3), the difference between H₂O₂ production for quartz and labradorite was not statistically significant
 161 (p = 0.87). Both labradorite and quartz are tectosilicates consisting of silica tetrahedra which share all
 162 four corners with a neighbouring tetrahedra in their crystal structure. Forsterite, an orthosilicate, with no
 163 shared corners between silica tetrahedra, had a significantly (p < 0.05) lower average peak H₂O₂
 164 concentration (39.1 ± 2.2 nmol g⁻¹; Figs. 2 & 3) than both labradorite and quartz. All H₂O₂ productive
 165 minerals exhibited a significant correlation (p < 0.05) between the temperature of abrasion and the
 166 amount of H₂O₂ produced (Fig. 2). Strikingly, the sign and strength of these correlations were not the
 167 same for each mineral; quartz and forsterite produced maximum concentrations when abraded at 193
 168 K and exhibited a negative trend with temperature (r_{quartz} = - 0.68, n = 12; r_{forsterite} = - 0.98, n = 12; Fig.
 169 2) whereas labradorite produced a maximum at 273 K and showed a positive trend with temperature (r_{labradorite} = 0.89, n = 12; Fig. 2). This result suggests that within single mineral species, the quantity of
 171 fine particulates generated (and by proxy, surface area) was not always the dominant control on net
 172 H₂O₂ generation in experiments.

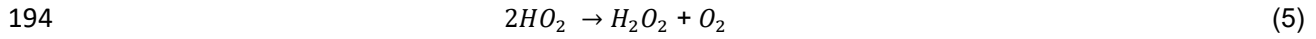
173 Hurowitz et al. (2007) suggested a relationship between the crystal structure of crushed silicates and
 174 the production of H₂O₂, with the number of corners shared by the basic silica tetrahedra determining
 175 H₂O₂ productivity. Opal is a poorly crystalline silicate; the X-ray diffraction pattern for the opal confirmed
 176 the weak crystallinity in these samples (Fig. S1). The lack of H₂O₂ generation in opal therefore supports
 177 the hypothesis that crystal structure is important in determining mineral oxidant production. However,
 178 Hurowitz et al. (2007) and Hendrix et al. (2019) noted an inverse relationship between shared corners
 179 of silica tetrahedra and ROS generation. The crystal structure of the productive minerals in our current
 180 study showed the opposite trend (Figs. 2 & 3).

181 One potential explanation for this disparity could be the maximum temperature reached during the
 182 milling process. High energy abrasion experiments (e.g. Hurowitz et al., 2007) have indicated that H₂O₂
 183 can form after grinding of minerals via the mechanical fracturing of silicate bonds and the subsequent
 184 reaction of the fresh, radical hosting silicate surfaces with water (Hendrix et al., 2019):



187 Kita et al. (1982) show that the SiO[•] radical is relatively stable and will not readily react with water until
 188 temperatures greater than ~ 493 K are reached, in excess of the controlled temperatures in this study.
 189 Strong correlations between atmospheric O₂ and H₂O₂ in low energy tumbling experiments by Bak et
 190 al. (2017) suggest that O₂ modification of the fresh silicate surfaces enables an alternative H₂O₂
 191 generation mechanism through the formation of superoxide radicals:

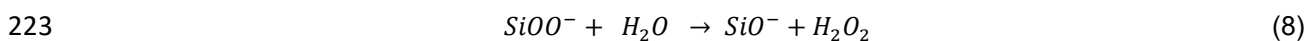
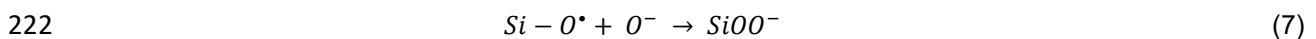
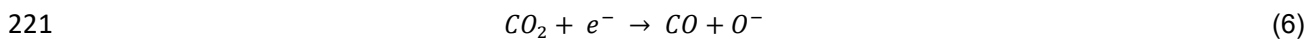




195 Tumbling experiments where O₂ levels were varied showed a strong correlation between H₂O₂
 196 production and atmospheric O₂ levels, suggesting O₂ is consumed by reactions 3 - 5 (Bak et al., 2017).
 197 Using the Ideal Gas Law, under the starting conditions reported in our study ($p_{O_2} = 10.5$ Pa, $V = 0.00025$
 198 m³, $R = 8.31$ J K⁻¹ mol⁻¹, $T = 293$ K) there was ~ 110 nmol of O₂ in the ampoules available to bond at
 199 the silicate surface prior to the addition of water, which contained ~1.44 μmol L⁻¹. From equations 3 –
 200 5, this could have resulted in a maximum production of ~ 7.0 nmol g⁻¹ H₂O₂ in our experiments; this
 201 equates to 6.0, 6.2 and 17.9% of maximum H₂O₂ yields for labradorite, quartz and forsterite respectively.
 202 We therefore conclude that only a fraction of the total H₂O₂ production in some of our experiments could
 203 have come from starting O₂. The average peak H₂O₂ concentration of the non-abraded controls was
 204 4.9 ± 0.5 nmol g⁻¹ (\pm SEM, $n = 48$; Appendix B), consistent with near quantitative consumption of O₂
 205 available in the ampoules at the start of experimentation. Any silica radicals not deactivated in the
 206 preparatory steps could have reacted with this O₂ and generated H₂O₂ via Eq's. 3 – 5.

207 One alternative source of H₂O₂ is from pre-existing peroxy linkages ($\equiv Si-O-O-Si \equiv$) within igneous
 208 silicate minerals (Balk et al., 2009). These defects, equivalent to two co-joined SiO[•], can be produced
 209 during the original cooling of a water-containing magmatic melt to form the silicate minerals (Balk et al.,
 210 2009). Under stress, these defects in the minerals can migrate through the crystal matrix to form surface
 211 SiO[•], and it has been further proposed that these can then form H₂O₂ via Eq. 2 (Balk et al., 2009).
 212 However, Kita et al (1982) demonstrated that silicate surface SiO[•] are stable to temperatures greater
 213 than ~ 493 K - well above the temperatures of our study. We also note that the experiments of Balk et
 214 al. (2009) were carried out under air at room temperature and hence the H₂O₂ generated in these
 215 experiments may instead have utilised O₂ (Eqs. 3 - 5).

216 Instead, we suggest that the additional source of oxygen in the abraded experiments is from the more
 217 abundant starting concentrations of CO₂. In prior tumbling experiments simulating Martian saltation,
 218 electrostatic discharges between grains, evidenced by triboluminescence from agitated abraded
 219 material, has been hypothesised to dissociate atmospheric species, including CO₂, providing a third
 220 H₂O₂ generation mechanism (Bak et al., 2017; Thøgersen et al. 2019):



224 Given the stability of the SiO[•] radical (Kita et al., 1982) at the temperatures recorded here and the
 225 insufficient availability of O₂ in the ampoules, we suggest that equations 6 – 8 were likely to dominate
 226 H₂O₂ generation in our study. The measurement of CO in future experiments (Eq. 6) would further help
 227 test this hypothesis. In prior high energy milling experiments, substantial heat will have been generated
 228 during high energy impacts, reducing the stability of the H₂O₂ generating intermediary - SiOO^{•/•-} (Kita et

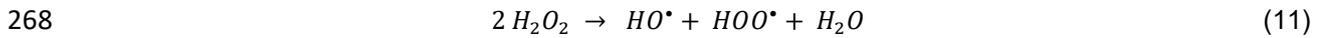
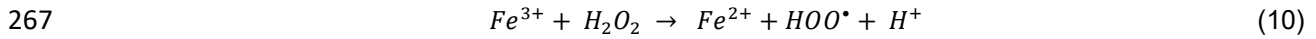
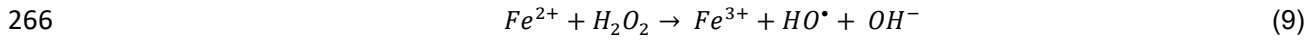
229 al., 1982; Yen et al., 2000). In contrast in our study the grinding temperature was carefully controlled to
230 low temperatures, allowing the build-up of $\text{SiOO}^{\cdot-}$ on mineral surfaces over time. This scenario is also
231 consistent with the results of Hendrix et al. (2019) where an inverse relationship was found between
232 grinding time and ROS generation, suggesting that increased temperature resulted in the
233 instability/reaction of oxidant generating mineral surface radical species.

234 Time series for each of the mineral phases allowed the evolution and stability of H_2O_2 to be monitored
235 (Fig. 3). In forsterite experiments, maximum H_2O_2 concentrations were recorded at 24 hours after the
236 addition of water, decreasing over 168 hours (Fig. 3). Maximum H_2O_2 concentrations in quartz
237 experiments were quantified within 5 minutes of the addition of water, decreasing over the subsequent
238 168 hours. A varnish-type material was also observed on the inside of the ampoules within which quartz
239 was abraded (Fig. S5), but not with other minerals. We suggest that this fine material/varnish would
240 have provided an enhanced surface area for reactions to proceed and could potentially explain the rapid
241 observed increase in H_2O_2 concentrations in the quartz samples. Uniquely, labradorite samples
242 consistently maintained H_2O_2 levels after an initial 24-hour increase through the end of the analytical
243 period (Fig. 3). Bak et al. (2017) suggested that silica radicals partake in both the generation and the
244 destruction of H_2O_2 ; the absence of any degradation of H_2O_2 in the labradorite samples could indicate
245 that secondary mineral phases formed on silica surfaces, depleting the available silica sites that could
246 consume H_2O_2 . Alternatively, the lack of iron in labradorite (Fig. S6) would also limit Fenton chemistry
247 (Hurowitz et al., 2007) which would consume H_2O_2 .

248 3.3 Iron availability and Fenton chemistry

249 Whilst forsterite was the only mineral abraded with iron in its chemical structure, dissolved iron was only
250 consistently recorded in samples from quartz experiments (maximum $0.86 \pm 0.16 \mu\text{mol L}^{-1}$; Figs. 4 &
251 S6). Iron measured in the residual liquids of the other minerals were below quantification except for one
252 forsterite sample abraded at 193 K, one labradorite sample abraded at 223 K and several opal samples
253 abraded above 223 K (LOQ = $0.11 \mu\text{mol L}^{-1}$; Fig. S6). Small quantities of a black magnetic mineral
254 below the level of detection with XRD analysis (LOQ ~ 1%; Fig S2) were observed in the initial quartz
255 substrate. There was a significant correlation between the concentration of dissolved iron and the
256 proportion of quartz abraded to fines ($r = 0.85$, $n = 12$, $p < .001$; Fig. 4) suggesting a relatively
257 homogenous distribution of the magnetic mineral within the quartz. In all cases, whilst both Fe^{2+} and
258 Fe^{3+} were measured, only Fe^{3+} was detected. This result is likely due to the nature of the oxidising
259 environment produced by H_2O_2 and other ROS generated in experiments, rapidly oxidizing any
260 dissolved Fe^{2+} .

261 Iron species can partake in Fenton-type reactions (Eq's. 9 - 11) in both the solid (heterogeneous) and
262 aqueous (homogeneous) phases. It is kinetically favourable for heterogeneous Fenton reactions to
263 proceed when suitable iron minerals are present as solid phases with aqueous H_2O_2 (Araujo et al.,
264 2011). Soluble Fe^{2+} and Fe^{3+} can subsequently enter the aqueous phase leading to simultaneous
265 homogeneous Fenton reactions propagating and enhancing the overall reaction (Araujo et al. 2011):



269 The measured H₂O₂ concentrations in experiments must thus be considered the net product of multiple
270 simultaneous productive and destructive reactions. The inverse relationships between H₂O₂ generation
271 and temperature of abrasion for forsterite and quartz samples can be explained by consideration of
272 competing H₂O₂ generating and consuming reactions (Fig. 2). At higher temperatures, minerals are
273 more susceptible to abrasion resulting in the generation of a higher number of silica radical sites and in
274 the case of Fe bearing minerals, a greater surface area for Fenton-type reactions to proceed. H₂O₂ is
275 generated by silica radical sites and consumed by Fe phases according to availability of both Fe²⁺ and
276 Fe³⁺. If the rate of consumption of H₂O₂ is greater than its rate of generation then H₂O₂ cannot
277 accumulate. In this study, H₂O₂ generation is suppressed for Fe bearing samples at higher abrasion
278 temperatures suggesting that either Fenton reactions are more efficient than silica radical – water
279 reactions under these conditions or that Fenton active species were generated at a faster rate than
280 silica radicals during the abrasion process.

281 3.4 Hydrogen generation

282 After exposure to water, each mineral type except opal generated detectable quantities of H₂ gas (MDL
283 = 2.2 nmol g⁻¹; Fig. S7). Labradorite and forsterite only produced H₂ slightly above detection (maximum
284 = 4.3 ± 0.4 and 3.4 ± 0.3 nmol g⁻¹ for labradorite and forsterite respectively; Fig. S7) and only at higher
285 temperatures of abrasion. In total, 7 out of 12 abraded quartz samples generated detectable H₂ after
286 the addition of water, with a maximum of 37.8 ± 3.7 nmol g⁻¹ at 223 K (Fig. 5a - 5c). In quartz samples
287 H₂ generation generally decreased as abrasion temperature increased to 273 K with no H₂ recorded at
288 193 K (Fig. 5a). There was unlikely any limitation through the accumulation of H₂ given the ample
289 headspace (~15 cm³) and H₂ concentrations were still increasing at 168 hours, suggesting equilibrium
290 conditions were not reached (Fig. 5c). The considerable variation within replicates in this study suggests
291 that abrasion temperature and fresh silica surface area were not the only variables affecting H₂
292 production. Crucially, H₂ was only present at the end of the experiment in quartz samples when the
293 liquid phase contained detectable dissolved Fe (MDL = 0.03 μmol L⁻¹; Fig. 5); above this concentration
294 dissolved Fe did not correlate with the amount of H₂ produced suggesting hydrolysis during dissolution
295 of the iron phase was not the source of H₂ (Fig. 5b).

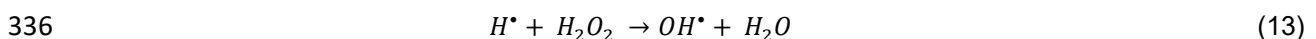
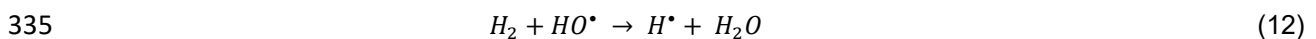
296 Previous experiments utilising natural rocks and minerals to investigate H₂ production have investigated
297 a number of different mechanisms of H₂ generation. Kita et al. (1982) examined how the presence of
298 O₂ during the milling of quartz altered H₂ yields; their study determined that milling in a pure water
299 vapour atmosphere generated significantly more H₂ than milling in moist air. This was attributed to the
300 formation of SiOO^{•/•-} through the reaction of Si[•] and SiO[•] with atmospheric oxygen species (O₂, O⁻),

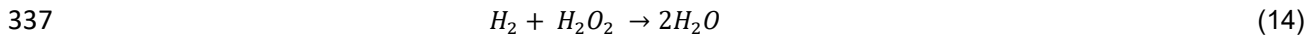
301 precluding H₂ generation from the reaction of Si[•] with H₂O. We suggest that our results are consistent
302 with the oxidation of Si[•] by starting oxygen and reactive oxygen species produced during abrasion (Eq.
303 6 - 8). Studies where crushing was performed in the absence of O₂ have produced H₂ with variable
304 yields (Stevens & McKinley, 2000; Neubeck et al., 2011, Mayhew et al., 2013). These studies have all
305 utilised iron bearing minerals although none of these studies controlled the minor mineral phases and
306 importantly, all of these studies prepared their mineral samples by crushing in air but did not measure
307 the production of potential oxidants alongside H₂ in their experiments.

308 Stevens & McKinley (2000) reported no detectable H₂ generation from the reaction of a magnetite (a
309 spinel) substrate with water whilst Mayhew et al. (2013) observed significant H₂ generation when 40 %
310 (modal abundance by volume) forsterite was present in a magnetite substrate. In the Mayhew et al.
311 (2013) model, H₂ is produced when electrons are transferred to water molecules and protons adsorbed
312 to spinel surfaces. Sustained H₂ production occurs when dissolved Fe species adsorb and donate
313 electrons to the spinel surface resulting in the continuous reduction of water and the generation of H₂.
314 This model is consistent with H₂ generation in our abraded quartz experiments where H₂ production
315 was initially rapid, then decreased but had not appeared to have plateaued after 168 hrs (Fig. 5c). We
316 suggest that spinel-promoted-electron transfer was a source of H₂ in the quartz samples and that
317 competition with oxidants generated from the reactions of SiOO^{•/•-} and water exerted a control on this
318 production. Dissolved Fe was not present above detection (MDL = 0.03 μmol L⁻¹) in the labradorite or
319 forsterite samples that generated H₂ and we suggest this limited H₂ generation (Fig. S7) was due to the
320 reaction of Si[•] with water. It is possible a fraction of the H₂ measured in the quartz samples was also
321 generated by this mechanism. The lack of detectable H₂ generated from amorphous opal potentially
322 indicates that mineral crystal structure exerts a control on H₂ as well as H₂O₂ generation.

323 3.5 Oxidant regulation of hydrogen generation

324 Concentrations of H₂ against H₂O₂ for quartz samples are plotted in Figure 6a (n = 36) for the three
325 comparable time points (0, 24, 168 hrs) investigated at all temperatures of abrasion (193, 223, 253, and
326 273 K). The determining component is the presence of dissolved Fe and thus the presence of an Fe
327 phase abraded from the quartz (Fig. 6b). Net H₂O₂ concentrations increased rapidly before returning to
328 close to detection at 168 hours. Conversely, H₂ accumulated in the headspace of quartz experiments
329 over 168 hours. Prior abrasion studies performed on pure quartz under Martian analogue conditions
330 have reported ~ 40 % yields of HO[•] radicals compared to H₂O₂ (Bak et al., 2017). This suggests a
331 significant portion of the oxidants produced within our study were not measured. In the presence of
332 available Fe²⁺, Reactions 9 – 11 will have further increased the concentration of ROS in the liquid. H₂
333 should readily react with HO[•] radicals and H₂O₂ via the series of reactions comprising the Allen chain
334 reaction (Allen et al., 1952), reducing H₂ yields:





338 Telling et al. (2015) reported a lag between the addition of water to some of their crushed rock samples
339 and net H₂ production; perhaps indicating these H₂ consuming redox reactions constrain low level net
340 H₂ production in low temperature environments. Figures 5 and 6b show that significant concentrations
341 of H₂ are only measured in quartz samples with dissolved Fe concentrations in excess of 0.03 μmol L⁻¹.
342 In quartz experiments where H₂O₂ was below detection (samples with a dissolved Fe content above
343 detection ~ 0.03 μmol L⁻¹), we infer that Fenton processes have inhibited the accumulation of H₂O₂.

344 We propose here an extended version of the Mayhew et al. (2013) model, where abraded samples
345 follow one of two reaction pathways that result in the generation of net H₂O₂ or net H₂ dependant on
346 the ratio of spinel surface area (H₂ production sites) to silica radical sites (H₂O₂ and H₂ production sites)
347 and the background concentration of Fe species (Fig. 7). This ratio is expressed by the generation and
348 destruction of H₂O₂ and H₂ through a balance of silica radical – water and silica oxide radical - water
349 reactions, Fenton reactions, spinel-surface-promoted-electron transfer as well as tertiary
350 oxidation/reduction reactions such as those described by Allen's chain reaction. In environments with
351 high spinel surface area to silica radical ratios, the production rate of H₂ (via electron transfer to water)
352 on spinel surfaces can exceed the production of ROS species at silica oxide radical sites, generating
353 net H₂. Conversely, when the spinel surface area to silica radical ratio is low, H₂O₂ generation rates
354 exceed H₂ production rates, resulting in the net accumulation of H₂O₂ (Fig 7). H₂O₂ and other ROS may
355 also oxidize the reactive spinel surfaces and inhibit H₂ generation. A summary of these reactions is
356 shown in Fig. 7.

357 3.6 Implications for Mars

358 3.6.1 Water and oxygen availability as a control on ROS production

359 The mechanisms for ROS production in our experiments are all dependent on the presence of liquid
360 water. Up to 29% of Mars' surface area has been modelled to experience pressures and temperatures
361 suitable to support liquid water (Harberle et al., 2001). This area increases if brines are considered,
362 which are capable of forming metastable liquids at a much larger range of temperatures and pressures
363 (Rivera-Valentin et al., 2020). Liquid water is predicted to form on Mars as thin films on the order
364 nanometres thick on mineral surfaces, becoming substantially thicker when films containing impurities
365 form (Boxe et al., 2012). In a model proposed by Yen et al. (2005), frosts are deposited at night before
366 rapidly sublimating in the morning. Any condensation in excess of a single monolayer however can
367 behave as a liquid, capable of mobilising ions from the regolith (Yen et al., 2005) and would potentially
368 be available for other water – rock interactions, including mineral surface radicals produced during
369 aeolian abrasion.

370 In our experiments, the amount of molecular oxygen available to react with mineral surface radicals
371 (Eq. 3) and other reduced species was limited, although a further source of oxygen might be available

372 from the triboelectric disassociation of CO₂ (Eq. 6; Bak et al., 2017). However, on the surface of Mars,
373 the substantial volume of the Martian atmosphere will potentially provide a non-limiting source of oxygen
374 over time to fuel continued oxidation. We therefore view our rates of oxidant production (after water
375 addition) as a lower limit.

376 3.6.2 Abrasion rate as a function of temperature

377 While the dissolution of minerals during the experiment precludes an accurate analysis of the different
378 abrasion rates with temperature, the varying mass of fine productions are consistent with a temperature
379 dependence of mineral resistance to abrasion. Further work directly investigating the mechanical
380 properties of minerals at Martian temperatures is ongoing to more robustly test this hypothesis. The
381 composition of aeolian deposits covering volcanic regions is often taken as the average composition of
382 the underlying bedrock (e.g. Stockstill-Cahill et al., 2008). Known aeolian processes can apply sorting
383 effects, systematically altering the composition of this sediment with respect to source rocks (Mangold
384 et al., 2011). We suggest investigation of Martian sedimentary sequences should consider the
385 temperature at which aeolian processes occurred as a further control on sorting and composition.

386 3.6.3 Mineral structure and Fe content as controls on oxidant production

387 The H₂O₂ production capacity of the silicates abraded in this study show a dependence on the crystal
388 structure of the abraded mineral as suggested by Hurowitz et al. (2007). In our study tectosilicates had
389 higher H₂O₂ production capacities than orthosilicates. Quartz commonly makes up < 2 % of the Martian
390 regolith, however labradorite and forsterite have been shown to comprise ~ 40 and ~ 20 % of the
391 crystalline component of the regolith respectively (Bish et al., 2013). Importantly, however, the inactivity
392 of the opal suggests the amorphous content of the Martian regolith does not contribute to its oxidising
393 nature through the mechanisms described here. Equally importantly, our results suggest that net H₂O₂
394 production can be regulated not only by mineral structure, but by the presence of Fe bearing mineral
395 species. Haematite, magnetite and nano-phase iron oxides are common on Mars (e.g. Bish et al., 2013).
396 Accordingly, net H₂O₂ production rates in the Martian regolith are liable to be limited by Fenton reactions
397 (with the consequent production of more reactive OH[•] and OOH[•] radicals; Eq. 9 - 11) in the presence
398 of suitable Fe bearing species.

399 3.6.4 The impact of aeolian driven oxidant production on organic matter preservation

400 The reactions involving the crystalline silicate phases described here are able to produce oxidising
401 environments that would impact on the preservation potential of any meteoritic or native organic material
402 in the Martian regolith. Liquid water may persist as brines for up to 6 hours at a time in some regolith
403 settings (Rivera-Valentin et al., 2020). Within this time frame, our data suggests the potential for mineral
404 driven H₂O₂ production, with the further potential for Fe species to partake in Fenton reactions, further
405 increasing the oxidative stresses and subsequent degradation of any organic species. Additional

406 experiments are required to quantify how fast these reactions can proceed at the low temperatures
407 representative of eutectic salt brines (Rivera-Valentin et al., 2020).

408 3.6.5 Insight into low temperature hydrogen generation

409 In support of previous studies (e.g. Kita et al., 1982) our results indicate that H₂ generated from the
410 reaction of Si[•] with water will be limited where oxygen is available to form SiOO^{•/•}. Our results further
411 show that spinel surface promoted electron transfer could be initiated on the Martian surface in the
412 presence of liquid water to produce H₂ gas (Mayhew et al., 2013). The lifetime of molecular H₂ in the
413 Martian atmosphere is measured in centuries, and unlike water vapour, H₂ can migrate through the
414 upper atmosphere where a proportion is dissociated and lost to space as H (Chaffin et al., 2017).
415 Oxidants such as H₂O₂ generated from abraded mineral-water reactions would inhibit net H₂ production;
416 limiting the loss of this H₂ into and from the Martian atmosphere.

417 We suggest that conflicts in the current literature regarding the potential for H₂ generation from water-
418 mineral reactions at low temperatures (Kita et al., 1982; Anderson et al., 1998; Telling et al., 2015;
419 Stevens & McKinley, 2000; Nuebeck et al., 2011; Mayhew et al., 2013), may at least in part be
420 reconciled by the contemporaneous production of H₂O₂ and ROS by the crushing of the studied
421 materials that inhibit net H₂ production; particularly those (the majority) of studies that have crushed
422 their experimental minerals under air.

423 4. Conclusions

424 Our study suggests that the level of resistance of different minerals to abrasion by simulated saltation
425 is temperature dependant with increased abrasion observed at warmer temperatures. After low energy
426 abrasion for 142 days, the crystalline silicate minerals quartz, labradorite and forsterite all generated
427 significant ($p < 0.05$) quantities of H₂O₂ on contact with water. The amorphous mineral opal however
428 did not generate any H₂O₂ supporting the hypothesis of Hurowitz et al. (2007) that there is a link between
429 mineral crystal structure and oxidant producing capacity. Our results further demonstrate that Fe-driven
430 Fenton chemistry will limit the net accumulation of H₂O₂ in silica radical - water reactions if appropriate
431 Fe species are available; presumably resulting in the production of more reactive ROS such as OH[•].
432 Further research is required to better quantify the rates of potential oxidant production on organic matter
433 preservation in sediments driven by the formation of transient brines on and in active aeolian sediment,
434 and potential interactions with UV irradiation.

435 Our paired analyses of H₂ alongside H₂O₂ production supports previous studies (e.g. Kita et al., 1982)
436 where H₂ generation is limited by the formation of SiOO^{•/•}, precluding the reaction of Si[•] with water. Our
437 results also suggest there may also be a link between mineral structure and H₂ generation. Finally, we
438 extend the model of Mahyew et al. (2013), in that spinel surface promoted electron transfer can result
439 in the net production of H₂ - but only if H₂O₂ (and presumably other ROS) have been reduced to close
440 to detection (here $\sim 2.9 \mu\text{mol L}^{-1}$). The production of ROS on crushed mineral surfaces may help provide

441 at least part of the explanation for prior conflicting experimental results and conclusions on the potential
442 for low temperature H₂ production from silicate-water reactions.

Funding: This work was supported by the UK Space Agency [grants ST/S001484/1 and ST/R001421/1]

Figures:

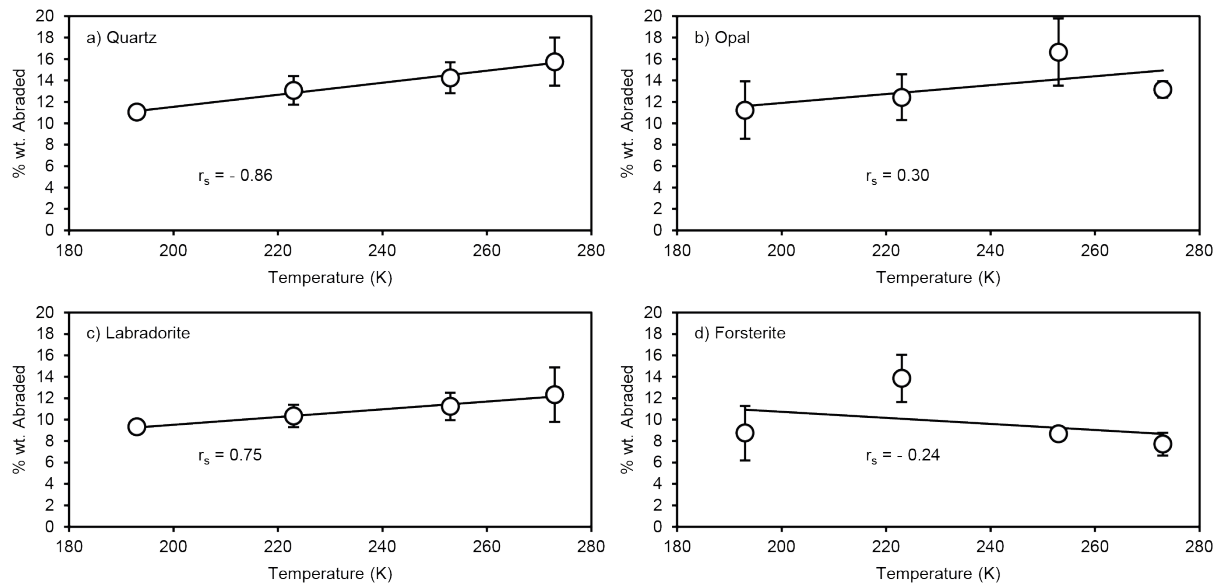


Figure 1: Percentage weight (wt. %) of a) quartz, b) opal, c) labradorite and d) forsterite abraded to less than 125 μm after 142 days of simulated saltation plotted against the temperature of abrasion in Kelvin (K). The strength of correlation for each plot is reported as the Spearman's rank correlation coefficient (r_s).

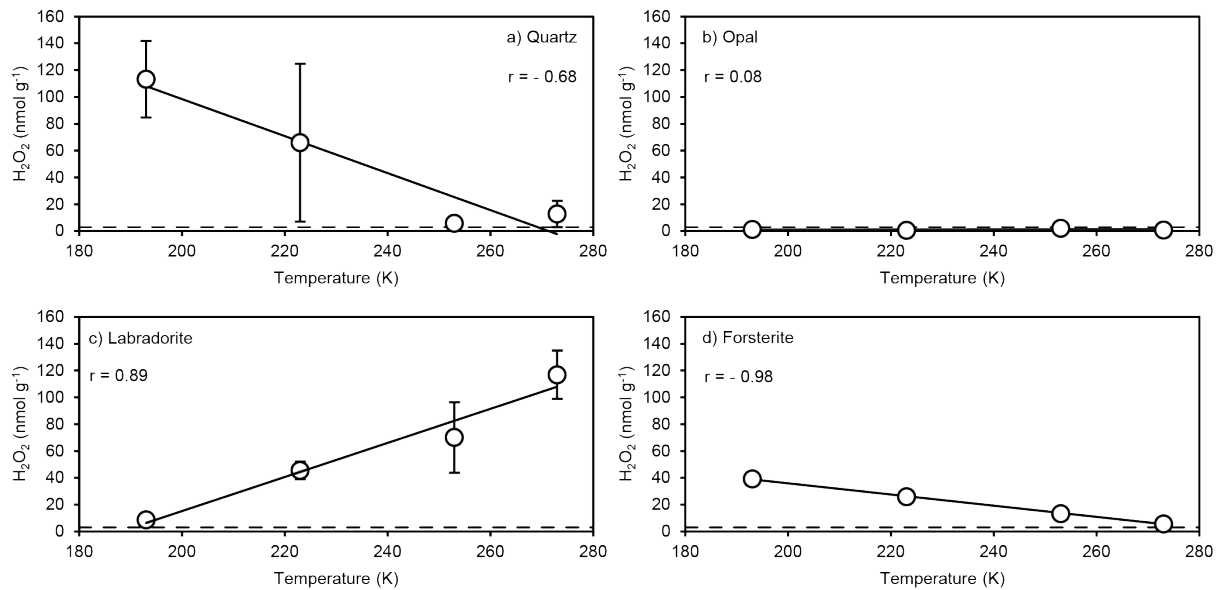


Figure 2: Net H_2O_2 generated (nmol g^{-1}) by abraded quartz, labradorite, opal, and forsterite after simulated saltation in a Martian atmosphere at 193 K, 223 K, 253 K and 273 K. The dashed line signifies the MDL (2.9 nmol g^{-1}). Minerals were abraded for 142 days and subsequently exposed to anoxic water. Error bars are shown as the SEM ($n=3$).

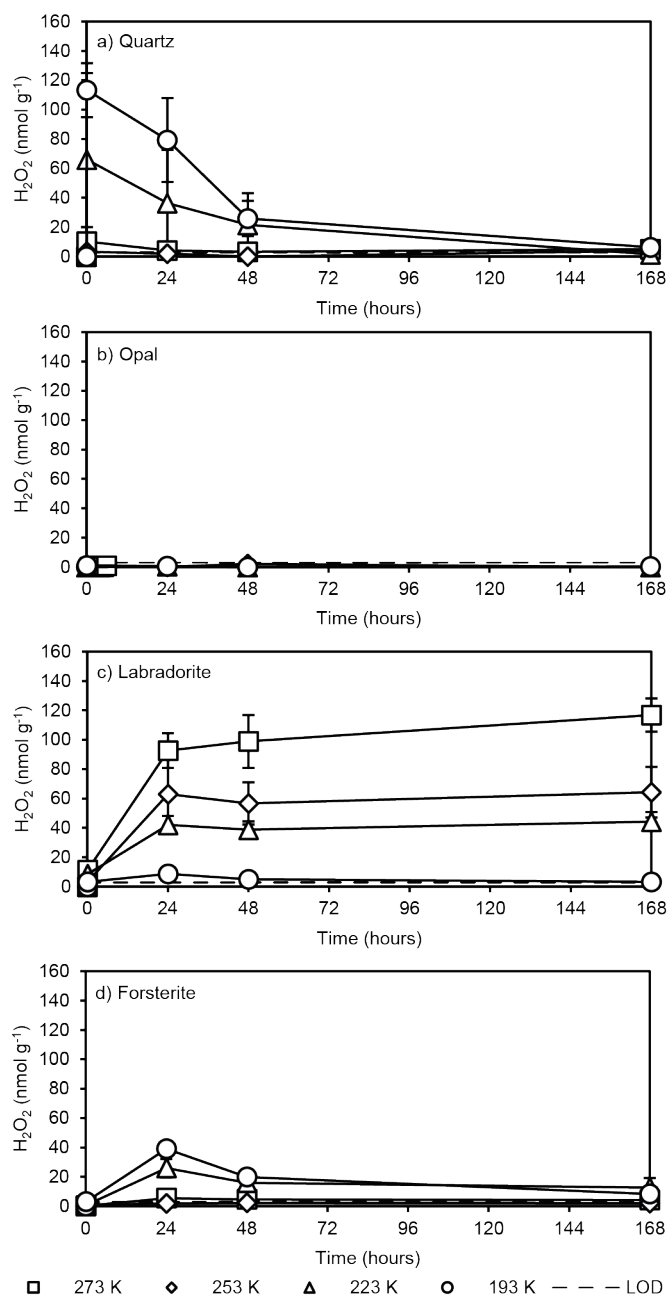


Figure 3: Time series of net H₂O₂ generation (nmol g⁻¹) by abraded: a) quartz b) opal c) forsterite and d) forsterite, at the four temperatures tested (see key). Minerals were abraded for 142 days in a simulated Martian atmosphere. The dashed line signifies the MDL (2.9 nmol g⁻¹). Error bars are shown as the SEM (n=3).

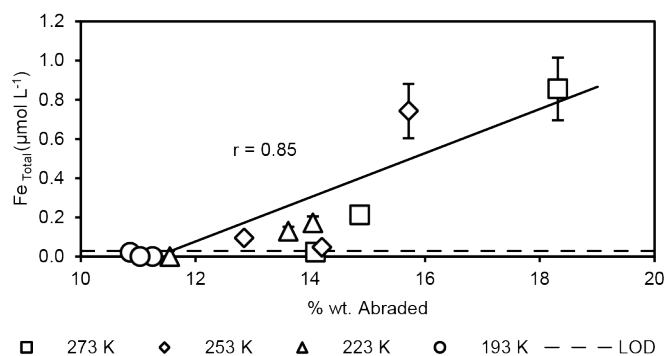


Figure 4: Concentration of total Fe in the residual liquids from quartz samples abraded in a Martian atmosphere for 142 days and exposed to anoxic water. Fe concentrations are plotted against the percentage weight of quartz abraded below 125 μm . The dashed line signifies the MDL ($0.03 \mu\text{mol L}^{-1}$) Error bars are shown as the maximum coefficient of variance of standards over the total calibration range (18.7 %).

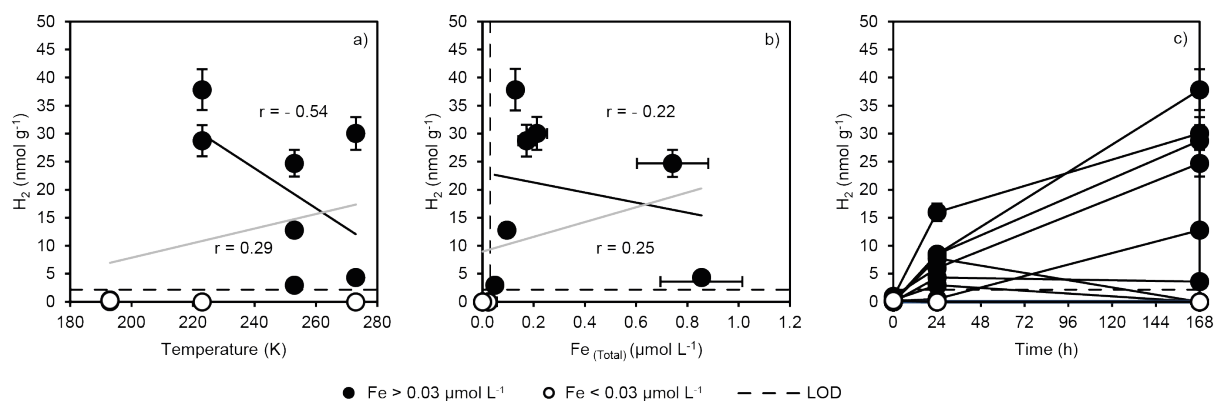


Figure 5: Net H_2 generated over 168 hours from quartz abraded for 142 days in a simulated Martian atmosphere and exposed to anoxic water. H_2 (nmol g^{-1}) is plotted a) against the temperature of abrasion (K) with lines of best fit between Fe bearing samples (black) and all samples (grey), b) against the concentration of total Fe with lines of best fit between Fe bearing samples (black) and all samples (grey), and c) as time series. The dashed lines signify the MDL ($0.03 \mu\text{mol L}^{-1}$ and 2.2 nmol g^{-1} for Fe and H_2 respectively). Each data point is a single experiment. Errors are given as the maximum coefficient of variance of standards over the total calibration ranges. Fe concentration of the liquid (above or below detection) from each sample is given in the key.

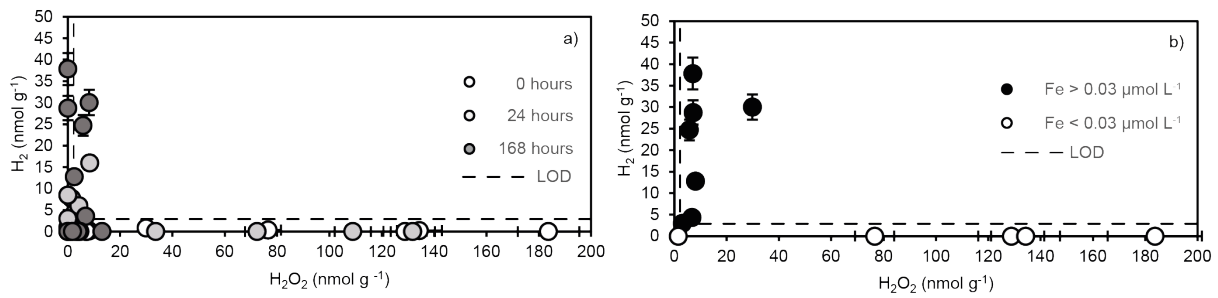


Figure 6: H₂ generation plotted against H₂O₂ generation from quartz abraded for 142 days in a simulated Martian atmosphere and exposed to anoxic waters: a) measurements for H₂ (nmol g⁻¹) and H₂O₂ (nmol g⁻¹) at time points 0, 24 and 168 hours. Each data point is a single pair of measurements at the stated time, b) H₂ (nmol g⁻¹) at the end of the experiment plotted against maximum measured H₂O₂ (nmol g⁻¹) (this plot is temporally inconsistent). Error bars are given as the maximum coefficient of variance of standards for each species calibration range.

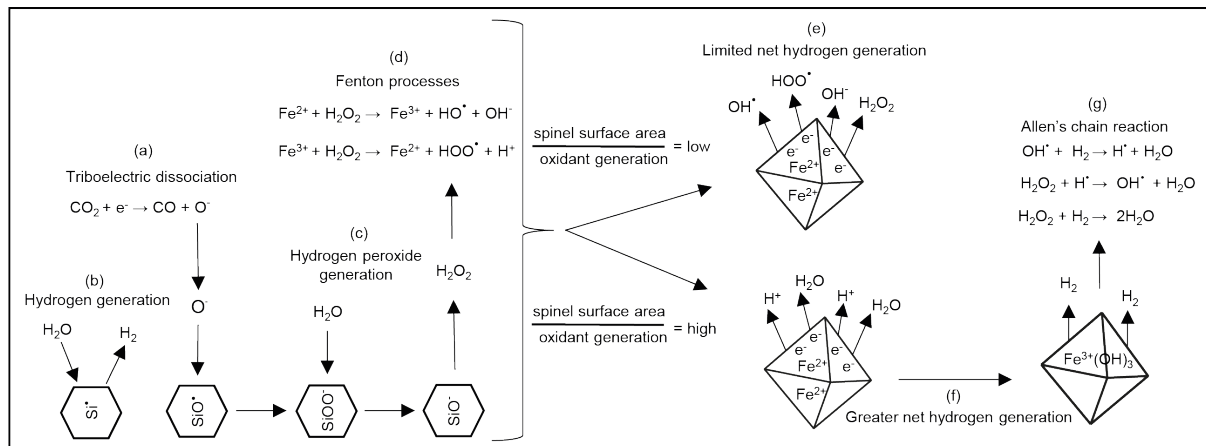


Figure 7: Reaction schematic showing the different processes described in text. a) electrical dissociation of CO₂ and reaction of O⁻ with abraded, b) generation of H₂ through the reaction of silica radicals with water, c) generation of H₂O₂ through the reaction of oxygen modified silica radicals with water, d) Fenton reactions, e) oxidants inhibit net H₂ generation, f) spinel-surface-promoted H₂ generation, and g) Allen's chain reactions.

5. References

1. Allen, A.O., Hochanadel, C., Ghormley, J. and Davis, T. (1952) 'Decomposition of water and aqueous solutions under mixed fast neutron and γ -radiation', *The Journal of Physical Chemistry*, 56(5), pp. 575-586.
2. Anderson, R.T., Chapelle, F.H., Lovley, D.R. (1998) 'Evidence Against Hydrogen-Based Microbial Ecosystems in Basalt Aquifers', *Science* 281, 976.
3. Araujo, F., Yokoyama, L., Teixeira, L., Campos, J. (2011) 'Heterogeneous Fenton process using the mineral hematite for the discolouration of a reactive dye solution'. *Brazilian Journal of Chemical Engineering*, 28, pp 605-616.
4. Atreya, S.K. and Gu, Z.G. (1994) 'Stability of the Martian atmosphere: Is heterogeneous catalysis essential?' *Journal of Geophysical Research: Planets*, 99(E6), pp. 13133-13145.
5. Atreya, S.K., Wong, A.-S., Renno, N.O., Farrell, W.M., Delory, G.T., Sentman, D.D., Cummer, S.A., Marshall, J.R., Rafkin, S.C. and Catling, D.C. (2006) 'Oxidant enhancement in martian dust devils and storms: implications for life and habitability', *Astrobiology*, 6(3), pp. 439-450.
6. Ayoub, F., Avouac, J.-P., Newman, C., Richardson, M., Lucas, A., Leprince, S. and Bridges, N. (2014) 'Threshold for sand mobility on Mars calibrated from seasonal variations of sand flux', *Nature communications*, 5(1), pp. 1-8.
7. Baga, A.N., Johnson, G.A., Nazhat, N.B. and Saadalla-Nazhat, R.A. (1988) 'A simple spectrophotometric determination of hydrogen peroxide at low concentrations in aqueous solution', *Analytica chimica acta*, 204, pp. 349-353.
8. Bak, E.N., Zafirov, K., Merrison, J.P., Jensen, S.J.K., Nørnberg, P., Gunnlaugsson, H.P. and Finster, K. (2017) 'Production of reactive oxygen species from abraded silicates. Implications for the reactivity of the martian soil', *Earth and Planetary Science Letters*, 473, pp. 113-121.
9. Balk, M., Bose, M., Ertem, G., Rogoff, D.A., Rothschild, L.J., and Freund, F.T. (2009) 'Oxidation of water to hydrogen peroxide at the rock-water interface due to stress-activated electric currents in rocks', *Earth and Planetary Science Letters*, 283, pp. 87-92
10. Biemann, K., Oro, J., Toulmin III, P., Orgel, L., Nier, A., Anderson, D., Simmonds, P., Flory, D., Diaz, A. and Rushneck, D. (1977) 'The search for organic substances and inorganic volatile compounds in the surface of Mars', *Journal of Geophysical Research*, 82(28), pp. 4641-4658.
11. Bish, D.L., Blake, D., Vaniman, D., Chipera, S., Morris, R., Ming, D., Treiman, A., Sarrazin, P., Morrison, S. and Downs, R. (2013) 'X-ray diffraction results from Mars Science Laboratory: Mineralogy of Rocknest at Gale crater', *science*, 341(6153), p. 1238932.
12. Boxe, C., Hand, K., Nealon, K., Yung, Y., Yen, A. and Saiz-Lopez, A. (2012) 'Adsorbed water and thin liquid films on Mars', *International Journal of Astrobiology*, 11(3), pp. 169-175.
13. Bridges, N., Ayoub, F., Avouac, J., Leprince, S., Lucas, A. and Mattson, S. (2012) 'Earth-like sand fluxes on Mars', *Nature*, 485(7398), pp. 339-342.
14. Bridges, N., Sullivan, R., Newman, C., Navarro, S., Van Beek, J., Ewing, R., Ayoub, F., Silvestro, S., Gasnault, O. and Le Mouélic, S. (2017) 'Martian aeolian activity at the Bagnold Dunes, Gale Crater: The view from the surface and orbit', *Journal of Geophysical Research: Planets*, 122(10), pp. 2077-2110.
15. Chaffin, M., Deighan, J., Schneider, N., Stewart, A. (2017) 'Elevated atmospheric escape of atomic hydrogen from Mars induced by high-altitude water' *Nature Geoscience* 10, 174.
16. Delory, G.T., Farrell, W.M., Atreya, S.K., Renno, N.O., Wong, A.-S., Cummer, S.A., Sentman, D.D., Marshall, J.R., Rafkin, S.C. and Catling, D.C. (2006) 'Oxidant enhancement in martian dust devils and storms: storm electric fields and electron dissociative attachment', *Astrobiology*, 6(3), pp. 451-462.
17. Eigenbrode, J.L., Summons, R.E., Steele, A., Freissinet, C., Millan, M., Navarro-González, R., Sutter, B., McAdam, A.C., Franz, H.B., Glavin, D.P. (2018) 'Organic matter preserved in 3-billion-year-old mudstones at Gale crater, Mars' *Science* 360, 1096-1101.

18. Encrenaz, T., Bézard, B., Greathouse, T., Richter, M., Lacy, J., Atreya, S., Wong, A., Lebonnois, S., Lefèvre, F. and Forget, F. (2004) 'Hydrogen peroxide on Mars: evidence for spatial and seasonal variations', *Icarus*, 170(2), pp. 424-429.
19. Evans, B. and Goetze, C. (1979) 'The temperature variation of hardness of olivine and its implication for polycrystalline yield stress', *Journal of Geophysical Research: Solid Earth*, 84(B10), pp. 5505-5524.
20. Goldich, S.S. (1938) 'A study in rock-weathering', *The Journal of Geology*, 46(1), pp. 17-58.
21. Haberle, R.M., McKay, C.P., Schaeffer, J., Cabrol, N.A., Grin, E.A., Zent, A.P. and Quinn, R. (2001) 'On the possibility of liquid water on present-day Mars', *Journal of Geophysical Research: Planets*, 106(E10), pp. 23317-23326.
22. Hecht, M., Kounaves, S., Quinn, R., West, S., Young, S., Ming, D., Catling, D., Clark, B., Boynton, W. and Hoffman, J. (2009) 'Detection of perchlorate and the soluble chemistry of martian soil at the Phoenix lander site', *Science*, 325(5936), pp. 64-67.
23. Hendrix, D.A., Port, S.T., Hurowitz, J.A. and Schoonen, M.A. (2019) 'Measurement of OH* Generation by Pulverized Minerals Using Electron Spin Resonance Spectroscopy and Implications for the Reactivity of Planetary Regolith', *GeoHealth*, 3(1), pp. 28-42.
24. Hurowitz, J.A., Tosca, N.J., McLennan, S.M. and Schoonen, M.A. (2007) 'Production of hydrogen peroxide in Martian and lunar soils', *Earth and Planetary Science Letters*, 255(1-2), pp. 41-52.
25. Iversen, J.D., Rasmussen, K.R. (1999) 'The effect of wind speed and bed slope on sand transport'. *Sedimentology* 46, 723-731.
26. Kita, I., Matsuo, S. and Wakita, H. (1982) 'H₂ generation by reaction between H₂O and crushed rock: An experimental study on H₂ degassing from the active fault zone', *Journal of Geophysical Research: Solid Earth*, 87(B13), pp. 10789-10795.
27. Kranjc, K., Rouse, Z., Flores, K.M. and Skemer, P. (2016) 'Low-temperature plastic rheology of olivine determined by nanoindentation', *Geophysical Research Letters*, 43(1), pp. 176-184.
28. Levin, G.V. and Straat, P.A. (1977) 'Recent results from the Viking labeled release experiment on Mars', *Journal of Geophysical Research*, 82(28), pp. 4663-4667.
29. Mahaffy, P.R., Webster, C.R., Atreya, S.K., Franz, H., Wong, M., Conrad, P.G., Harpold, D., Jones, J.J., Leshin, L.A. and Manning, H. (2013) 'Abundance and isotopic composition of gases in the Martian atmosphere from the Curiosity rover', *Science*, 341(6143), pp. 263-266.
30. Mangold, N., Baratoux, D., Arnalds, O., Bardintzeff, J.-M., Platevoet, B., Grégoire, M., Pinet, P. (2011). Segregation of olivine grains in volcanic sands in Iceland and implications for Mars. *Earth and Planetary Science Letters*, 310, pp. 233-243.
31. Martínez, G., Newman, C., De Vicente-Retortillo, A., Fischer, E., Renno, N., Richardson, M., Fairén, A., Genzer, M., Guzewich, S. and Haberle, R. (2017) 'The modern near-surface Martian climate: A review of in-situ meteorological data from Viking to Curiosity', *Space Science Reviews*, 212(1-2), pp. 295-338.
32. Mayhew, L.E., Ellison, E., McCollom, T., Trainor, T. and Templeton, A. (2013) 'Hydrogen generation from low-temperature water-rock reactions', *Nature Geoscience*, 6(6), pp. 478-484.
33. Merrison, J. (2012) 'Sand transport, erosion and granular electrification', *Aeolian Research*, 4, pp. 1-16.
34. Neubeck, A., Duc, N.T., Bastviken, D., Crill, P. and Holm, N.G. (2011) 'Formation of H₂ and CH₄ by weathering of olivine at temperatures between 30 and 70 C', *Geochemical Transactions*, 12(1), p. 6.
35. Nørnberg, P., Bak, E., Finster, K., Gunnlaugsson, H., Iversen, J., Jensen, S.K., Merrison, J. (2014). 'Aeolian comminution experiments revealing surprising sandball mineral aggregates'. *Aeolian Research*, 13, pp. 77-80.
36. Oyama, V.I. and Berdahl, B.J. (1977) 'The Viking gas exchange experiment results from Chryse and Utopia surface samples', *Journal of Geophysical Research*, 82(28), pp. 4669-4676.
37. Richardson, M.I., Toigo, A.D. and Newman, C.E. (2007) 'PlanetWRF: A general purpose, local to global numerical model for planetary atmospheric and climate dynamics', *Journal of Geophysical Research: Planets*, 112(E9).

38. Rivera-Valentín, E.G., Chevrier, V.F., Soto, A. and Martínez, G. (2020) 'Distribution and habitability of (meta) stable brines on present-day Mars', *Nature astronomy*, 4(8), pp. 756-761.
39. Stockstill-Cahill, K.R., Anderson, F.S., Hamilton, V.E. (2008). A study of low-albedo deposits within Amazonis Planitia craters: Evidence for locally derived ultramafic to mafic materials. *Journal of Geophysical Research: Planets*, p. 113.
40. Stevens, T.O. and McKinley, J.P. (2000) 'Abiotic Controls on H₂ Production from Basalt–Water Reactions and Implications for Aquifer Biogeochemistry', *Environmental Science & Technology*, 34(5), pp. 826-831.
41. Sullivan, R. and Kok, J. (2017) 'Aeolian saltation on Mars at low wind speeds', *Journal of Geophysical Research: Planets*, 122(10), pp. 2111-2143.
42. Telling, J., Boyd, E., Bone, N., Jones, E., Tranter, M., MacFarlane, J., Martin, P., Wadham, J., Lamarche-Gagnon, G. and Skidmore, M. (2015) 'Rock comminution as a source of hydrogen for subglacial ecosystems', *Nature Geoscience*, 8(11), p. 851.
43. Thøgersen, J., Bak, E.N., Finster, K., Nørnberg, P., Jakobsen, H.J., Jensen, S.J.K. (2019). 'Light on windy nights on Mars: A study of saltation-mediated ionization of argon in a Mars-like atmosphere'. *Icarus*, 332, pp. 14-18.
44. Viollier, E., Inglett, P., Hunter, K., Roychoudhury, A. and Van Cappellen, P. (2000) 'The ferrozine method revisited: Fe (II)/Fe (III) determination in natural waters', *Applied geochemistry*, 15(6), pp. 785-790.
45. Weigle, J.M. (1949) 'Crushing Strengths of Minerals at Low Temperatures', *Science*, 109(2827), pp. 229-230.
46. Yen, A., Kim, S., Hecht, M., Frant, M. and Murray, B. (2000) 'Evidence that the reactivity of the martian soil is due to superoxide ions', *Science*, 289(5486), pp. 1909-1912.
47. Yen, A.S., Gellert, R., Schröder, C., Morris, R.V., Bell III, J.F., Knudson, A.T., Clark, B.C., Ming, D.W., Crisp, J.A., Arvidson, R.E. (2005) An integrated view of the chemistry and mineralogy of Martian soils. *Nature*, 436, 49.

Appendix A: Supplementary Information

Mineral phase identification using X-ray Diffraction

Mineral phase identification was performed by X-Ray Diffraction utilising a PANalytical X'Pert Pro MPD, powered by a Philips PW3040/60 X-ray generator fitted with an X'Celerator detector. Diffraction data were acquired by exposing powder samples to Cu-K α X-ray radiation, which has a characteristic wavelength (λ) of 1.5418 Å. X-rays were generated from a Cu anode supplied with 40 kV and a current of 40 mA. Data sets were collected over a range of 3-85° 2 θ with a step size of 0.0167° 2 θ and nominal time per step of 500 seconds, using the scanning X'Celerator detector (hence the long counting time per step) and a secondary graphite crystal monochromator in the diffracted beam path. Fixed divergence and anti-scatter slits of ½° and 1°, respectively, were used together with a beam mask of 10 mm, soller slits of 0.04 radians, and all scans were carried out in 'continuous' mode.

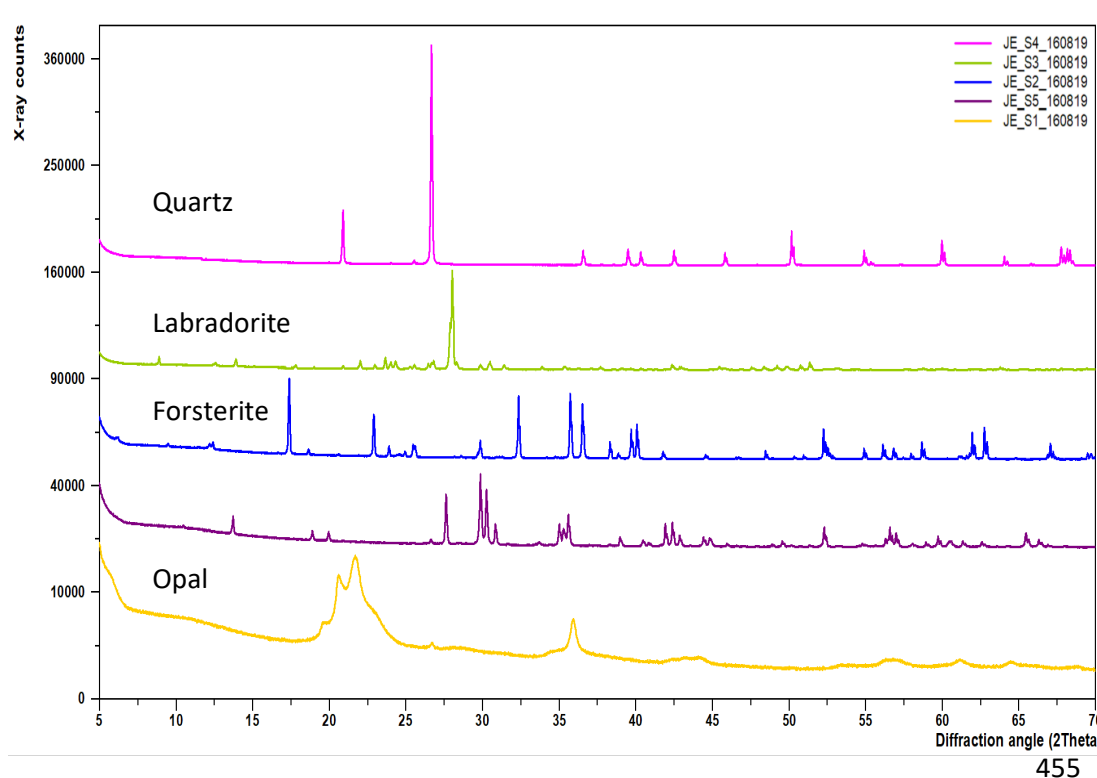


Figure S1: X-ray diffraction patterns for each of the minerals in this study shown over the range 5 - 70° 2 θ . Phase identification was carried out by means of the X'Pert accompanying software program PANalytical HighScore Plus in conjunction with the ICDD Powder Diffraction File 4 - Minerals (2019), the ICDD Powder Diffraction File 2 Database (2004) and the Crystallography Open Database (July 2016; www.crystallography.net). The above traces have been identified as quartz (pink), labradorite (green), forsterite (blue) and opal (yellow). The purple trace is pyroxene which was not used in this study.

Appendix A Supplementary Information

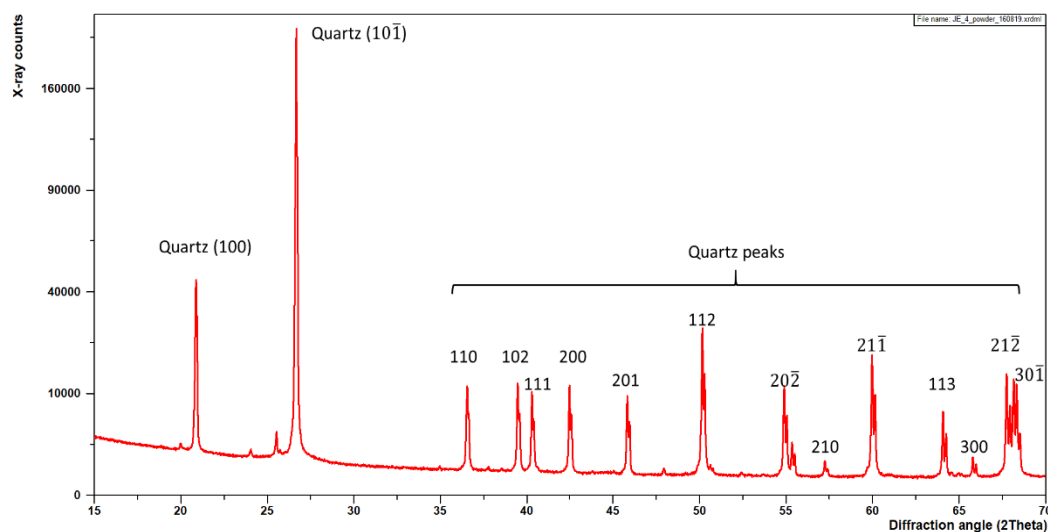


Figure S2: X-ray diffraction pattern for the quartz samples analysed here. Peaks are labelled according to their miller indices. Any minor mineral phases present were below detection $\sim 1\%$ and could not be confidently assigned.

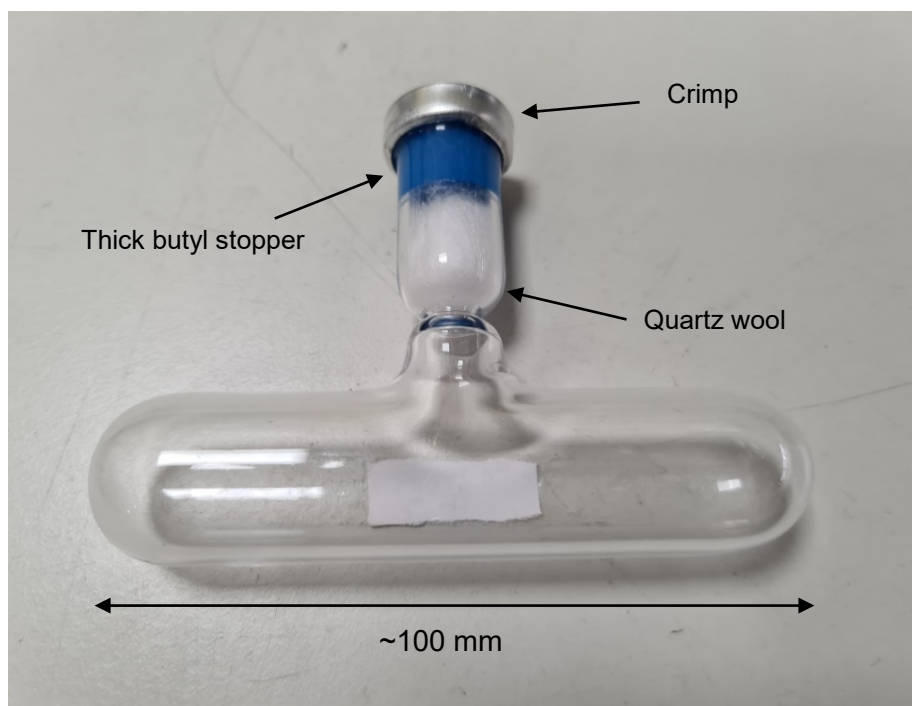


Figure S3: ~ 100 mm long quartz ampoules with constricted neck. Quartz wool placed at the constriction prevents the minerals contacting the thick butyl stopper. Ampoules were crimp sealed after the minerals were loaded and the internal gases exchanged through the stopper by needle. The white rectangle is a sample label on the exterior of the ampoule.

Appendix A: Supplementary Information



Figure S4: Ampoules were loaded onto metal plates which were fitted to the rotator axel. The axel passed through factory adapted ports in the sides of the incubators, in this fashion the electric rotator could safely be sited outside of the extremes of temperature. Temperatures were monitored with probes passed through the same ports.



Figure S5: Varnish type material adhered to the inside of the ampoule, typical of abraded quartz samples. This sample had low H_2O_2 levels (max = $6.6 \pm 0.4 \text{ nmol g}^{-1}$), moderately high H_2 (max = $24.7 \pm 2.4 \text{ nmol g}^{-1}$) and high $\text{Fe}_{(\text{Total})}$ ($0.74 \pm 0.1 \text{ } \mu\text{mol L}^{-1}$).

Appendix A: Supplementary Information

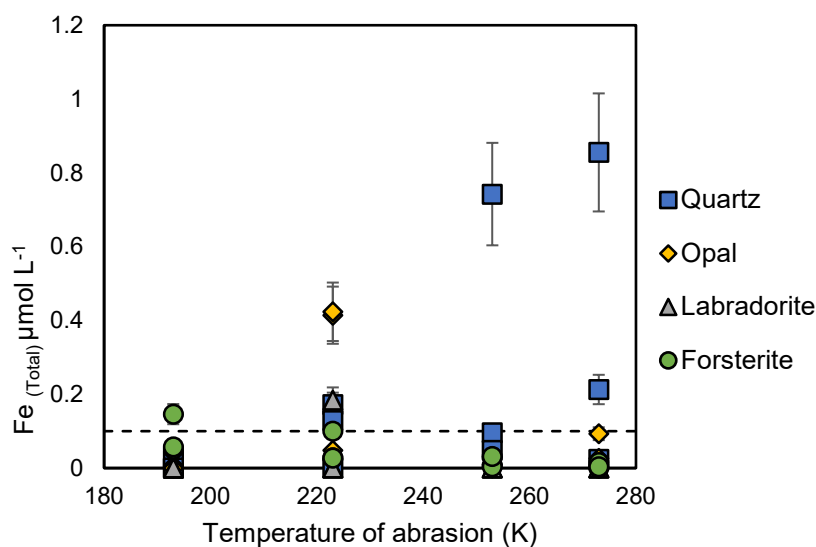


Figure S6: Concentration of $\text{Fe}_{(\text{Total})}$ in the residual liquids of each sample after 168 hours at the four temperatures analysed (193 K, 223 K, 253 K and 273K). Only quartz samples consistently contained Fe concentrations above the level of quantification ($0.11 \mu\text{mol L}^{-1}$). The dashed line signifies the limit of quantification. The symbols for each of the different minerals are given in the key and error bars are given as the maximum coefficient of variance across the full calibration range = 18.7 %.

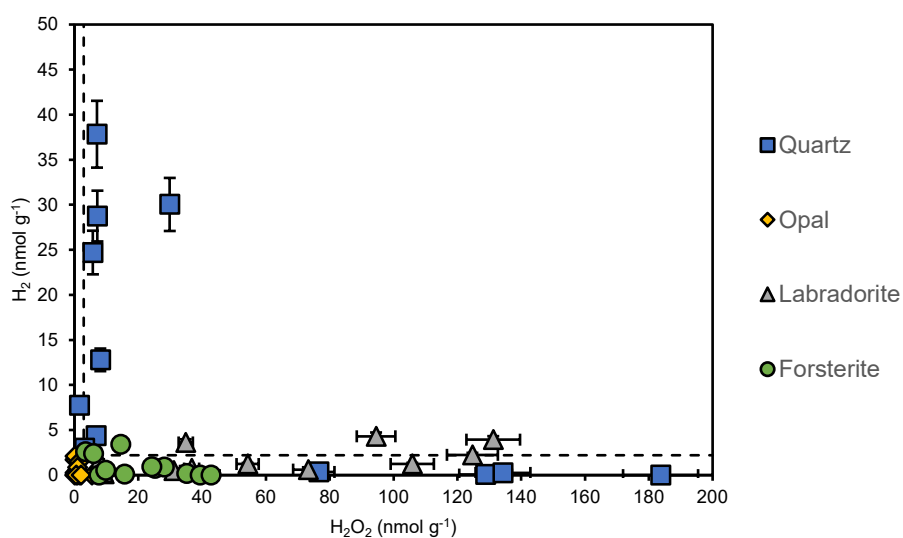


Figure S7: Maximum hydrogen plotted against maximum hydrogen peroxide for all mineral phases. Labradorite and forsterite generated minimal H_2 . Quartz samples containing a black magnetic minor Fe phase generated significant hydrogen (max = $37.8 \pm 3.7 \text{ nmol g}^{-1}$). Error bars are given as the maximum coefficient of variance over the calibration range for each chemical species (9.8 % and 6.4 % for hydrogen and hydrogen peroxide respectively). The dashed lines signify the method detection limits of 2.2 nmol g^{-1} and 2.9 nmol g^{-1} for hydrogen and hydrogen peroxide respectively. As these are maximum values this plot is temporally inconsistent – H_2 and H_2O_2 were not measured simultaneously above the level of quantification in the same sample at the same time point.

B Appendix B: Control experiments

The controls in this experiment were designed to distinguish between processes due to abrasion and those due to the contact of non-abraded minerals with water. Controls were treated in an identical manner to experimental samples except for the abrasion process.

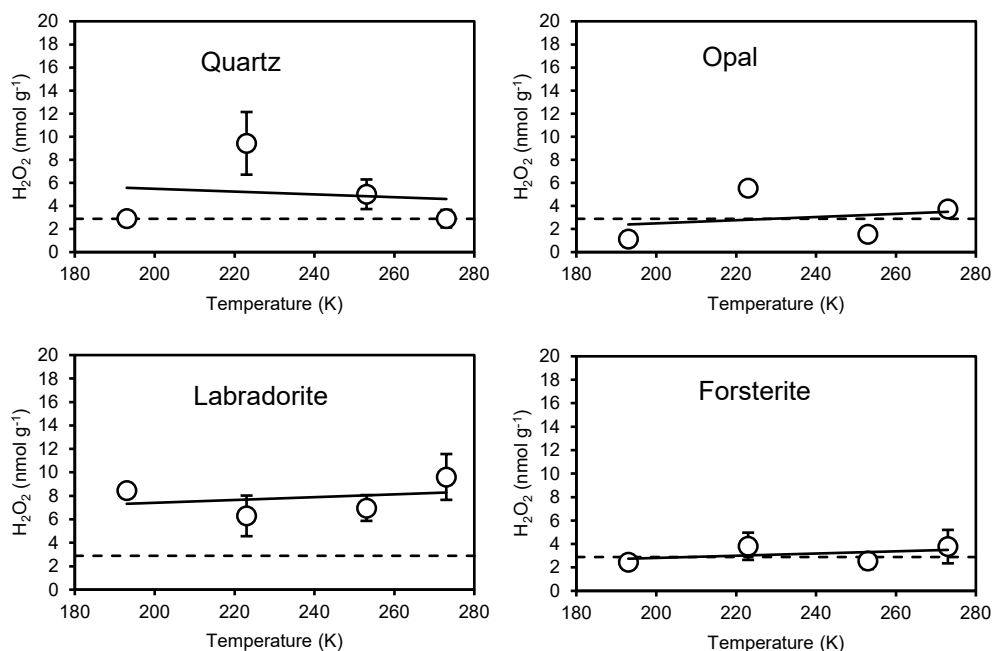


Figure B1: Hydrogen peroxide generation from control samples plotted against the temperature they were stored at for 142 days. The dashed lines show the method detection limit ($\text{MDL} = 2.9 \text{ nmol g}^{-1}$), calculated from the standard deviation of the water-blanks. Error bars are given as the maximum coefficient of variance across the calibration range (9.8 % and 6.4 % for hydrogen and hydrogen peroxide respectively)

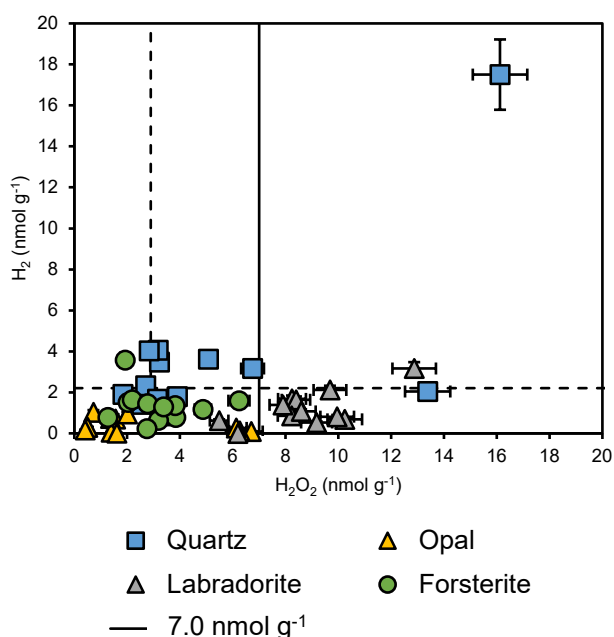


Figure B2: Hydrogen generation plotted against hydrogen peroxide generation for each non-abraded mineral control. We calculated there was $\sim 7.0 \text{ nmol g}^{-1}$ of oxygen (shown by the solid line) available from the added atmosphere in the ampoules at the start of the experiment and the water added after abrasion. The dashed lines signify the MDL of 2.2 nmol g^{-1} and 2.9 nmol g^{-1} for H_2 and H_2O_2 respectively. We suggest that this oxygen reacted with surface radicals activated by the crushing process and not deactivated by the washing and heating processes. The anomalously high data point had a dissolved Fe content of $0.13 \mu\text{mol L}^{-1}$, all of the other control sample Fe contents were below detection ($0.03 \mu\text{mol L}^{-1}$).

